

Spectroscopic diagnostics of low-ionized iron-peak elements. Electron-impact excitation of Ni^{3+} and photoionization of Ni^{2+} .

L. Fernández-Menchero, R. T. Smyth, C. A. Ramsbottom and C. P. Ballance

*Centre of Theoretical Atomic, Molecular and Optical Physics. Queen's University Belfast.
University Road, Belfast, BT7 1NN, Northern Ireland, United Kingdom*

Accepted XXX. Received YYY; in original form ZZZ

ABSTRACT

The spectra from Fe-peak elements may be used to determine the temperature and density of various astrophysical objects. Determination of these quantities is underpinned by the accuracy and the comprehensiveness of the underlying atomic structure and collisional calculations. In the following paper, we shall focus specifically on Ni IV lines associated with transitions amongst several low-lying levels. We shall employ modified versions of the parallel Dirac R-matrix codes, considering both electron-impact excitation of Ni^{3+} and the photoionisation of both the ground and excited states of Ni^{2+} . We produce high-quality data sets for both processes, and using these data, we calculate line ratios relevant for plasma diagnostics of temperature and density.

Key words: Atomic data – opacity – photoionization – electron-impact excitation

1 INTRODUCTION

The spectra of lowly ionized iron-peak elements such as (Fe^{q+} , Co^{q+} , Ni^{q+} , $q = 0 - 3$) are vitally important in astronomical observation. In particular, Ni^{3+} being iso-electronic with Fe^+ , should produce many of the same diagnostic lines, which have extensively been studied previously by Pradhan & Berrington (1993); Zhang & Pradhan (1995); Ramsbottom et al. (2005, 2007); Ramsbottom (2009). Comparisons of these lines using the results of the present paper shall be made. The Fe-peak elements provide some of the most abundant species created inside the stars, and they emit at ultraviolet wavelengths, making them dominant contributors to the opacity of the interstellar media under certain conditions.

From an atomic physics perspective, the half-open d-shell nature of many of these systems inevitably leads to target descriptions involving between twenty and thirty configurations if spectroscopic accuracy is to be approached. The $N + 1$ -electron collisional calculation, whether it be excitation or photoionisation expands to target descriptions involving between five- and seven-thousand levels with the associated cost of calculating over 10^9 Racah angular coefficients. Only with the development of the current suite of codes, including multiple layers of hyper-threaded parallelism, the Hamiltonian formation being the most critical part, have we been able to make progress on these type of systems. It has enabled us to provide comprehensive data sets that include *every* excitation and de-excitation for electron-impact excitation (EIE) or photoionisation (PI), not just from the ground state, but as well from *every* excited state.

Several groups throughout the world (The Opacity Project

Team 1995)¹, OPAL (Iglesias & Rogers 1996)², recognise that calculated opacities are essential for the correct interpretation of the spectra taken from a variety of objects, such as interstellar clouds, nebulae, remains of supernovae and stellar atmospheres. Even today, there are still remaining outstanding issues with experimental measurements that do not agree with any of the predicted models listed above (Bailey et al. 2014). We note that fundamental atomic data is only one aspect of the complex plasma-modelling codes, but the ability to put a realistic uncertainty on first principle calculations can eliminate it as the cause of disagreement with experimental observations. This has spurred the calculation of uncertainties with every collisional process, that are both a function of temperature and density. Our long-term goal is to ensure that the astrophysical modelling packages such as CLOUDY (Ferland et al. 2017)³, Xstar⁴ can integrate not only new atomic collisional data but also the associated uncertainty file.

One long-term project that recognised the need for comprehensive photoionisation of every ion stage for a large part of the periodic table is the Opacity Project (The Opacity Project Team 1995). The distribution of work on various atomic species was calculated by theoretical physics groups across the world and provided a very fruitful collaboration. However, as the near-neutral species are highly complex and the former computational resources were insufficient to calculate them, the Opacity Project saw a greater focus on the more highly ionised systems. With the exception of iron,

¹ <http://cdsweb.u-strasbg.fr/topbase/TheOP.html>

² <https://opalopacity.llnl.gov/>

³ <https://www.nublado.org>

⁴ <https://heasarc.nasa.gov/lheasoft/xstar>

and several large scale LS resolved models, comprehensive level resolved calculations involving several hundred states remain to be calculated for the near-neutral Fe-peak elements.

Currently within the literature, some of the following works represent historical attempts at calculating lowly-ionized iron peak elements, namely [Pradhan & Berrington \(1993\)](#); [Zhang & Pradhan \(1995\)](#) calculated the EIE of Mn-like Fe^+ in an LS coupling formalism. Their close-coupling expansion employed only three configurations, resulting in 38 LS terms, enabling transitions only among the ground and first excited configurations. We appreciate the limitations of this small model, and also that it has taken another twenty years to include twenty more configurations in the configuration-interaction (CI) description of our present model. [Ramsbottom et al. \(2005, 2007\)](#); [Ramsbottom \(2009\)](#) also within an LS -coupling framework made a succession of calculations with a progressively better target description. They ultimately included orbitals up to $n = 4$ resulting in a total of 113 LS terms in their close coupling (CC) expansion. Other set of works for other iso-electronic sequences of low-ionized iron peak elements includes the one of [Zhang & Pradhan \(1997\)](#) for EIE of Fe^{3+} , and [Bautista \(2004\)](#) for EIE of Ni^+ .

Although not as dominant as iron, nickel lines are also used for diagnostic and modeling of astrophysical plasmas. [Mazzali et al. \(2001\)](#) performed several models for type Ia supernovae concluding that nickel abundance can affect its brightness and decline rate. Years later, nickel lines were observed in the remnant of the supernova 1987A by [McCray & Fransson \(2016\)](#). Furthermore, [Werner et al. \(2018\)](#) subsequently used the absorption features in white dwarf atmospheres produced by iron-peak elements to model the metal abundances. Opacity data are necessary for any kind of simulation work so the demand for comprehensive data sets is almost insatiable. One such example of these simulations is the work of [Sánchez et al. \(2007\)](#). They used models dependent upon opacities and the known optical depths of the interstellar clouds to determine its fractal dimension. Another example is the work of [Moravveji \(2016\)](#), whose opacity simulations, comparing measured to measured spectra, concluded that nickel ions produce an enhancement of the opacity.

Opacity is also an important aspect of the `CLOUDY` software package ([Ferland et al. 2017](#)). `CLOUDY` is extensively used for the simulation of the spectra collected from interstellar clouds.

For completeness, the present work will investigate the Mn-like ion Ni^{3+} for two important processes: the EIE and the PI of its parent ion Ni^{2+} . We employ a heavily modified parallel version of the fully-relativistic Dirac Atomic R-matrix code (DARC) ([Norington & Grant 1987](#); [Ballance & Griffin 2004](#))⁵. We include 23 configurations in the CI expansion. This expansion leads to a total of 6841 relativistic levels. From that total, we reduce the CC expansion to include the first 262 levels, this reduction of the basis set may lead to pseudoresonances, and we have to take in account this fact when analysing the final collision strengths. Ni^{3+} is a low-ionized intermediate-mass ion, therefore there is the expectation that relativistic effects will not be large, especially for valence-shell electrons. One might argue on theoretical grounds that a semi-relativistic formalism, or even a non-relativistic one, would lead to acceptable results with considerably less computational effort. However, the current multi-level parallelism of the parallel DARC suite of codes, whilst being more computationally intensive is cur-

rently considerably more efficient than Breit-Pauli or ICFT semi-relativistic versions.

Over the last few years considerable effort has been made by the group at Queen's University Belfast in refactoring codes, specifically in terms of memory management. The last versions of the DARC code are viable, factoring in hardware limitations, to handle thousands of target states in the CC expansion.

The remainder of the paper is organized as follows: in Section 2 we give our description of the atomic structure; in Section 3 we describe the close-coupling method used to obtain the EIE collision strengths and subsequent effective collision strengths as well as the PI cross sections; in Section 4 we show and discuss the results; in Section 5 we perform a simple collision-radiative model to test the diagnostics predicted with present collision rates in relation to Fe II work; and in Section 6 we discuss the conclusions of the work. Atomic units are used unless otherwise specified.

2 STRUCTURE

We use the General-purpose Relativistic Atomic Structure Package (GRASP) ([Dyall et al. 1989](#); [Parpia et al. 1996](#)) to determine the best possible atomic structure within a Dirac-Coulomb framework. The resulting radial orbitals from this Multi-Configuration Dirac-Fock (MCDF) method are defined on an exponential radial grid and they are employed subsequently in the electron-impact excitation calculation.

In our CI expansion we permute the 25 electrons of the Mn-like Ni target within the configurations given below. Thirteen non-relativistic orbitals, namely the 1s, 2s, 2p, 3s, 3p, 3d, 4s, 4p, 4d, 5s, 5p, 6s, 6p are transformed into their relativistic counterparts within GRASP. To optimise the CI expansion and to accelerate the MCDF process we follow several steps, validating our results against the recommended values of the NIST atomic spectra data table ([Kramida et al. 2018](#); [Sugar & Corliss 1985](#)) where available. In our first step, we included the ground state configuration $Ne\ 3s^2\ 3p^6\ 3d^6\ 4s$, and all possible one-electron excitations $3s^2\ 3p^6\ 3d^6\ nl$. This simple expansion led to a first approximation of the one-electron wave functions. Additional configurations only slightly refine the core orbitals up to the 3s, but do help the convergence of the valence orbitals. With each iteration we check the updated excitation energies of the first 50 levels with the recommended data of NIST, with the goal of a compact but accurate basis. The results of our final 23 configuration model are listed in Table 1, though here we only provide a representative sample of the possible 6841 relativistic levels, the supplementary online material shall be more comprehensive. Comparing our calculated excitation energies with respect to the ground level with the recommended values of NIST we find our largest deviation in the order 12%, and an average deviation of 3.3%. This deviation is quite acceptable considering the complexity of the system and comparisons with the previous works for Mn-like Fe of [Ramsbottom et al. \(2005\)](#), whose largest deviation was order 15% in LS coupling, and the one of [Pradhan & Berrington \(1993\)](#), order 25%.

For a further comparison and to quantify the uncertainty in the atomic structure we performed a second independent calculation using a different atomic structure code. The `AUTOSTRUCTURE` program ([Badnell 2011](#)) code serves this purpose. `AUTOSTRUCTURE` provides non-relativistic radial wave functions from a Thomas-Fermi-Amaldi potential for the 1s to 6p orbitals. The subsequent Breit-Pauli Hamiltonian includes the relativistic terms as a first order perturbations: mass-velocity, spin-orbit and Darwin. We neglect

⁵ <http://connorb.freeshell.org>

Table 1. Configuration list included in the atomic structure calculations

Even parity		Odd parity
Core: $1s^2 2s^2 2p^6 3s^2$		
$3p^6 3d^6 4s$	$3p^5 3d^7 4p$	$3p^6 3d^5 4s 4p$
$3p^6 3d^7$	$3p^5 3d^7 5p$	$3p^6 3d^6 4p$
$3p^6 3d^5 4s^2$	$3p^4 3d^7 4s^2$	$3p^6 3d^6 5p$
$3p^6 3d^5 4p^2$	$3p^5 3d^7 6p$	$3p^6 3d^6 6p$
$3p^6 3d^6 5s$	$3p^6 3d^5 4d^2$	$3p^5 3d^7 4s$
$3p^6 3d^5 5s^2$	$3p^6 3d^6 4d$	$3p^5 3d^6 4s^2$
$3p^6 3d^5 5p^2$	$3p^4 3d^9$	$3p^5 3d^7 5s$
$3p^6 3d^6 6s$		$3p^5 3d^7 6s$

Table 2. Scaling parameters optimised by AUTOSTRUCTURE

1s	1.42396	4s	1.04299
2s	1.30959	4p	1.04410
2p	1.12342	4d	1.55730
3s	1.10133	5s	1.07620
3p	1.06211	5p	1.03593
3d	1.04845	6s	1.02930
		6p	1.01296

the second order perturbation terms spin-spin, orbit-orbit and spin-other-orbit. To determine the λ_{nl} , or scaling parameters within the TFA model potential, we variationally determine them from minimization of the absolute Hamiltonian energy. For a balanced comparison with the GRASP and DARC calculations and in order to minimise the differences in atomic structure, we keep both problems as similar as possible. In that regard, we include in the CI expansion of the AUTOSTRUCTURE model exactly the same configuration set as that in GRASP. After performing the minimization process we obtained the values of λ_{nl} shown in Table 2. In the supplementary online material we show the energies obtained with AUTOSTRUCTURE for a complete comparison with the ones obtained with GRASP and in Table 3 we show here the lowest-energy 50 levels. The level energies obtained with AUTOSTRUCTURE deviate slightly further from the recommended values of NIST than the ones obtained with GRASP. The maximum deviation is of the order of 15%, again larger than the GRASP one.

To perform the close-coupling (CC) integration including all the 6 841 levels obtained in the atomic structure is beyond the capabilities of existing workstations and even supercomputers. Consequently, we have selected the lowest excited 262 levels for the CC expansion. For analysis that favours the ground state and first few metastable states the completeness of this CC expansion is acceptable.

The online material will present a table of oscillator f strengths and Einstein spontaneous emission coefficients A for all the transitions between the 262 lowest-excited levels. We show the values obtained with both methods GRASP and AUTOSTRUCTURE. This comparison gives an idea of the consistency for energies and transition probabilities for both atomic models. We also compare our results for the Einstein A-coefficients with previous theoretical calculations in the literature from Hansen et al. (1984). Unfortunately, to the best of our knowledge there are no experimental data available in the scientific literature for Ni^{3+} to compare with.

Finally, to perform the scattering calculation we have shifted our calculated energies for the levels included in the CC expansion to the observed values of the NIST data base. Doing so we

make sure that the calculated wave lengths for the transitions will fit exactly with the observed ones, which is the requested for proper modelling of the astrophysical objects. In the NIST database, Ni^{3+} has some missing energy levels for the highly excited states. Therefore, in those cases we have shifted our theoretical values by the difference with respect to the known NIST levels. We compare our final results using the shifted target energies with the unshifted ones as a test of accuracy.

3 SCATTERING AND PHOTOIONIZATION PROCESSES

We use an R -matrix formalism (Hummer et al. 1993; Berrington et al. 1995). In the inner region, we use the fully relativistic DARC code (Ait-Tahar et al. 1996; Norrington & Grant 1981, 1987) to get the stationary solutions of the $N+1$ electron atom. We calculate the $N+1$ wave functions by diagonalization of the $N+1$ electron Hamiltonian. In addition, we calculate the dipole momentum matrices for the relevant photoionization transitions. In the outer region, we use the parallel version of the STGF program to calculate the EIE collision strengths Ω , and the radiative damped version PSTGBF0DAMP for the photoionization cross sections.

We calculate the photoionization cross sections from several initial states of the parent ion Ni^{2+} . These levels are the relevant ones for an opacity model. With the available computational resources it is absolutely impossible to include in the close coupling (CC) expansion all the 6 841 levels calculated with the previous described CI expansion in GRASP. To have a reasonable accuracy in the calculation compatible with an affordable computation cost we have selected the 262 levels with the lowest energy for the CC expansion.

We use the same set of 262 levels to calculate the electron-impact excitation of Ni^{3+} . We include partial waves with angular momentum up to $J = 36$.

3.1 Inner region

For our DARC calculation the R -Matrix inner-region radius is set to 59.52 a.u.. We calculate the Hamiltonian matrices and the transition dipole momentum matrices. Including the first 262 levels of Ni^{3+} target in the CC expansion we get a maximum of 1 818 channels in each J^π symmetry.

For the photoionization calculation we calculate partial waves with a total angular momentum of $J = 0 - 5$ and both parities. The lowest levels of the Ni^{2+} ion have an angular momentum of $J = 0 - 4$ and even parity (see Kramida et al. (2018)). Levels with higher angular momenta are very excited and they will rapidly decay to lower J by an M1 or E2 transition. Levels with odd parity are very high in energy, the first one is the $3p^6 3d^7 4p^5 F_5^o$ with an energy of 1.0043 Ry relative to the ground state. They will be connected by an E1 transition to any lower level with even parity and their population will be zero in any astrophysical object. In addition, for each partial wave we calculate the dipole matrices with all their possible E1 couples.

For the electron-impact excitation calculations we need a more extended set of partial waves. We have calculated the energies and wave functions of the channels of all partial waves with an angular momentum of $J = 0 - 36$ and both parities plus a top-up.

Table 3. Excitation energies of the first 50 Ni^{3+} target levels included in the present calculations

<i>i</i>	Configuration	Term	<i>J</i>	parity	GRASP	AS	NIST	Err GRASP (%)	Err AS (%)
1	$3p^6 3d^7$	4F	9/2	even	0.0	0.0	0.0	–	–
2	$3p^6 3d^7$	4F	7/2	even	1094.5	1210.7	1189.7	–8.0	1.8
3	$3p^6 3d^7$	4F	5/2	even	1889.7	2083.7	2042.5	–7.5	2.0
4	$3p^6 3d^7$	4F	3/2	even	2431.3	2675.5	2621.1	–7.2	2.1
5	$3p^6 3d^7$	4P	5/2	even	18113.0	19394.3	18118.6	0.0	7.0
6	$3p^6 3d^7$	4P	3/2	even	18459.6	19720.9	18366.8	0.5	7.4
7	$3p^6 3d^7$	4P	1/2	even	18956.7	20317.5	18958.4	0.0	7.2
8	$3p^6 3d^7$	2G	9/2	even	21941.1	22190.3	19829.6	10.6	11.9
9	$3p^6 3d^7$	2G	7/2	even	22987.4	23331.6	20947.6	9.7	11.4
10	$3p^6 3d^7$	2P	3/2	even	25818.1	26220.2	23648.9	9.2	10.9
11	$3p^6 3d^7$	2P	1/2	even	27106.1	27641.0	24651.4	10.0	12.1
12	$3p^6 3d^7$	2D_a	5/2	even	27855.5	28316.3	27096.5	2.8	4.5
13	$3p^6 3d^7$	2D_a	3/2	even	29754.2	30453.3	28777.7	3.4	5.8
14	$3p^6 3d^7$	2H	11/2	even	29856.6	30654.6	26649.1	12.0	15.0
15	$3p^6 3d^7$	2H	9/2	even	30766.3	31664.1	27677.6	11.2	14.4
16	$3p^6 3d^7$	2F	5/2	even	46822.8	48435.5	43437.5	7.8	11.5
17	$3p^6 3d^7$	2F	7/2	even	47307.1	48984.3	43858.6	7.9	11.7
18	$3p^6 3d^7$	2D_b	3/2	even	69463.3	71680.0	67360	3.1	6.4
19	$3p^6 3d^7$	2D_b	5/2	even	70208.8	72545.1	67989.8	3.3	6.7
20	$3p^6 3d^6 (^5D) 4s$	6D	9/2	even	104016.8	113059.3	110410.6	–5.8	2.4
21	$3p^6 3d^6 (^5D) 4s$	6D	7/2	even	104714.6	113865.8	111195.8	–5.8	2.4
22	$3p^6 3d^6 (^5D) 4s$	6D	5/2	even	105229.8	114458.9	111763.3	–5.8	2.4
23	$3p^6 3d^6 (^5D) 4s$	6D	3/2	even	105586.0	114868.0	112151.9	–5.9	2.4
24	$3p^6 3d^6 (^5D) 4s$	6D	1/2	even	105795.5	115108.6	112379.3	–5.9	2.4
25	$3p^6 3d^6 (^5D) 4s$	4D	7/2	even	116491.5	125023.6	120909.5	–3.7	3.4
26	$3p^6 3d^6 (^5D) 4s$	4D	5/2	even	117298.8	125960.5	121807.7	–3.7	3.4
27	$3p^6 3d^6 (^5D) 4s$	4D	3/2	even	117832.2	126574.9	122386.1	–3.7	3.4
28	$3p^6 3d^6 (^5D) 4s$	4D	1/2	even	118139.8	126928.8	122717.4	–3.7	3.4
29	$3p^6 3d^6 (^3P_a) 4s$	4P	5/2	even	135512.9	144723.7	139289.4	–2.7	3.9
30	$3p^6 3d^6 (^3P_a) 4s$	4P	3/2	even	135781.1	145030.5	139619.2	–2.7	3.9
31	$3p^6 3d^6 (^3H) 4s$	4H	13/2	even	136008.9	145290.5	139886.7	–2.8	3.9
32	$3p^6 3d^6 (^3P_a) 4s$	4P	1/2	even	136201.8	145512.5	140140.9	–2.8	3.8
33	$3p^6 3d^6 (^3H) 4s$	4H	11/2	even	138011.2	147167.4	138446.2	–0.3	6.3
34	$3p^6 3d^6 (^3F_a) 4s$	4F	9/2	even	139513.2	148730.2	141220.3	–1.2	5.3
35	$3p^6 3d^6 (^3H) 4s$	4H	7/2	even	139826.4	149097.6	141577.2	–1.2	5.3
36	$3p^6 3d^6 (^3H) 4s$	4H	9/2	even	139836.5	149191.9	140343	–0.4	6.3
37	$3p^6 3d^6 (^3F_a) 4s$	4F	7/2	even	140084.8	149395.2	141832	–1.2	5.3
38	$3p^6 3d^6 (^3F_a) 4s$	4F	5/2	even	140286.6	149629.3	142023.5	–1.2	5.4
39	$3p^6 3d^6 (^3F_a) 4s$	4F	3/2	even	140979.3	150489.1	141561.2	–0.4	6.3
40	$3p^6 3d^6 (^3P_b) 4s$	2P	3/2	even	142408.9	151421.3	144815.1	–1.7	4.6
41	$3p^6 3d^6 (^3G) 4s$	4G	11/2	even	143189.5	152259.5	145702.2	–1.7	4.5
42	$3p^6 3d^6 (^3G) 4s$	4G	9/2	even	143424.1	152637.1	145962.5	–1.7	4.6
43	$3p^6 3d^6 (^3G) 4s$	4G	7/2	even	143641.9	152973.0	146194.3	–1.7	4.6
44	$3p^6 3d^6 (^3G) 4s$	4G	5/2	even	143766.9	153187.4	146061.5	–1.6	4.9
45	$3p^6 3d^6 (^3H) 4s$	2P	1/2	even	143846.5	153267.4	146153.8	–1.6	4.9
46	$3p^6 3d^6 (^3H) 4s$	2H	11/2	even	145813.1	154764.1	145192.1	0.4	6.6
47	$3p^6 3d^6 (^3H) 4s$	2H	9/2	even	147063.6	156007.6	147635.9	–0.4	5.7
48	$3p^6 3d^6 (^3F_b) 4s$	2F	7/2	even	147768.3	156833.6	148358.2	–0.4	5.7
49	$3p^6 3d^6 (^3F_b) 4s$	2F	5/2	even	147948.1	157127.4	–	–	–
50	$3p^6 3d^6 (^3D) 4s$	4D	3/2	even	150422.2	159451.6	151574.7	–0.8	5.2

Key: *i*: level index; Conf: dominant electron configuration; Term: dominant LS term; *J*: level angular momentum; GRASP: present GRASP calculation, AS: present AUTOSTRUCTURE calculation; NIST: recommended value from NIST data base (Kramida et al. 2018); %: deviation respect the recommended values of NIST, in percentage. All energies in cm^{-1} .

3.2 Outer region

To calculate the photoionization cross sections as a function of photon energy in Rydbergs we utilise the parallel version of PSTGBF0-DAMP, a code which calculates the photoionization cross sections utilizing the previously calculated bound-free matrix elements. The first serial version of STGBF0DAMP was by Gorczyca and Badnell (unpublished). The first stage is to determine the bound levels of the

$(N + 1)$ -electron system Ni^{2+} in the program STGB (Seaton 1982; Berrington et al. 1987), which reads the wave functions for a specific partial wave in the inner region and determines its bound states. In our final calculated cross sections, we shift the energies of the numerical Ni^{2+} levels to fit exactly the ionization potential with the values tabulated in NIST data basis. Hence the threshold of the

cross sections fit exactly with the ionization potential of the initial state.

We split the energy range into two regions. In the low-energy region we adopt a fine energy mesh of $1.5 \times 10^{-5} z^2$ Ry, being $z = 3$ the charge of the final ion, to properly resolve the resonance structures converging onto the target thresholds. A linear grid with a total of 40 000 energy points was included up to the excitation energy of the last level included in the close-coupling expansion. Above this threshold resonances are not present and the cross sections are smoother, hence a coarser mesh of $3 \times 10^{-3} z^2$ Ry was utilised. For higher photon energies, above the excitation of the last included level in our CC expansion, 5.5 Ry in our case, there are more possible processes present in nature, for example the ionization with a final level which is not included in our CC expansion, or double ionization. Higher excited states, for example excitations $3s^{-1}$, while included in the CI expansion, are not included in the CC. Due to the limitation of our CC expansion, these processes can not be reproduced by our model. Hence present results are valid for a maximum photon energy of 5.5 Ry, approximately twice the ionization energy of Ni²⁺ from its ground level.

For the electron-impact excitation evaluation the parallel version of the STGF undamped package (Seaton *et al.*, unpublished) was utilised in the outer region. PSTGF calculates the outer-region wave function using a Numerov method and including the coupling in the outer-region as a perturbation. PSTGF joins the calculated wave function with one in the inner region in terms of the *R*-Matrix method (Burke 2011). In the outer region problem high angular momenta do not contribute to the resonance structures, hence we restrict the fine-mesh calculation to the low partial waves with $J = 0 - 20$ and adopt a fine energy mesh of $1.5 \times 10^{-5} z^2$ Ry, $z = 3$ being the ion charge, we incorporate a total of 40 000 points in the low energy region. At higher energies, above the threshold energy of the last level included in the CC expansion, there is no more resonance structure and the cross sections are smooth, so we use a coarser mesh of $3 \times 10^{-3} z^2$ Ry. The higher angular momenta $J = 21 - 36$ do not contribute to the resonance structure, even for low energies, hence the coarse mesh listed above is sufficient in the whole energy range. Finally, to include the remaining angular momenta up to J infinity we perform a top-up procedure. For dipole allowed transitions we use the Burgess sum rule Burgess (1974) and for the non-dipole allowed transitions with non-zero infinite energy Born limit a geometric series Badnell & Griffin (2001).

As the selected CC expansion in the target is considerably smaller than the initial CI expansion, we expect pseudoresonances to appear for electron final energies larger than the energy of the last level included in the CC expansion (2.57 Ry), equivalent to an electron temperature of 8×10^5 K. As the peak-abundance temperature of Ni³⁺ in a collisional plasma is 4×10^4 K (Bryans *et al.* 2006), these pseudoresonances will not affect the effective collision strengths at temperatures where Ni³⁺ has a significant ionisation fraction. Nevertheless, we have checked for the relevant transitions, the collision strengths these pseudoresonances are present.

4 RESULTS

4.1 Electron-impact excitation of Ni³⁺

The collision strength (Ω_{ij}) between an initial state i and a final state j is directly related to the electron-impact collisional excita-

tion cross section σ_{ij} by

$$\sigma_{ij} = \Omega_{ij} \frac{\pi a_0^2}{\omega_i k_i^2}, \quad (1)$$

where $\omega_i = 2J_i + 1$ is the statistical weight of level i and k_i^2 is the incident electron energy in Rydberg. In the majority of astrophysical plasmas the electron velocity distribution is Maxwellian for a certain temperature T . Hence to aid plasma modeling we have performed a convolution of the collision strength Ω_{ij} in terms of the Maxwellian distribution to obtain the associated effective collision strengths Υ_{ij} .

$$\Upsilon_{ij} = \int_0^\infty \Omega_{ij}(E_j) \exp\left(-\frac{E_j}{kT}\right) d\left(\frac{E_j}{kT}\right) \quad (2)$$

where T is the Maxwellian electron temperature in K, E_j is the final energy of the incident electron and k is Boltzmann's constant. For high temperatures the Maxwellian has a long tail and it is necessary to calculate Ω_{ij} up to a suitably high energy. This requires the inclusion of a large number of continuum states in the Hamiltonian and thus increase the corresponding size of the matrices beyond the computation capabilities available. To alleviate this problem we have calculated, using DARC, the infinite-energy limit for the electric dipole transitions and interpolated Ω_{ij} in the scaled Burgess-Tully domain Burgess & Tully (1992) between the last energy calculated in the outer region with PSTGF and the infinite energy point. For the present calculation we can therefore guarantee accuracy of the Υ_{ij} up to the order of 5.5 Ry, equivalent to 2×10^6 K. The temperature of maximum-abundance for Ni³⁺ is approximately 5×10^4 K Maz-zotta *et al.* (1998); Bryans *et al.* (2006), which indicates that the present evaluation is sufficient to model and resolve the emission features of the Ni IV lines in the range of temperatures where Ni³⁺ is abundant. We have used the program ADASEXJ (Griffin and Badnell, unpublished) to perform the convolution of the Ω and calculated the Maxwellian Υ . We create a level-resolved specific ion ADF04 file to store all the relevant collision-radiative parameters. This ADF04 file can be used as standard input to usual collision-radiative modelling software, for example the ADAS series 2 (Summers 1994).

In the present work we have computed collision strengths Ω_{ij} and effective collision strengths Υ_{ij} for the electron-impact excitation of the Ni³⁺ ion for transitions between the lowest 262 levels, a total of 34 191 forbidden and allowed lines. The highest energy considered was 5.5 Ry, adequate when compared to the ionization energy of 4.037 Ry Kramida *et al.* (2018). Above this ionization energy, the collision strengths follow an asymptotic behaviour and can be interpolated with the infinite energy limit point in the Burgess-Tully domain Burgess & Tully (1992).

In Figure 1, we present the collision strength Ω_{ij} for the electron-impact excitation of some selected transitions of the Ni³⁺ ion. For all transitions we observe the expected series of resonances in the low energy region converging onto the target state thresholds included in the CC expansion, and a background above this that depends on the type of transition considered. The most useful transitions for astrophysical diagnosis are the M1 transitions between the levels of the ground term. A peculiarity of the present system is that the first levels with odd parity are highly excited, the first one listed as level 65. As a consequence of this the electric dipole E1 allowed transitions from the ground term are paradoxically very weak in comparison with the other M1 and E2 transitions within the lower-excited levels, in fact it is in this transition where both versions of the calculation, with shifted and unshifted target energies, disagree the most (panel (g)). The cause of this disagreement is that in both versions of the calculation, the wave functions of the

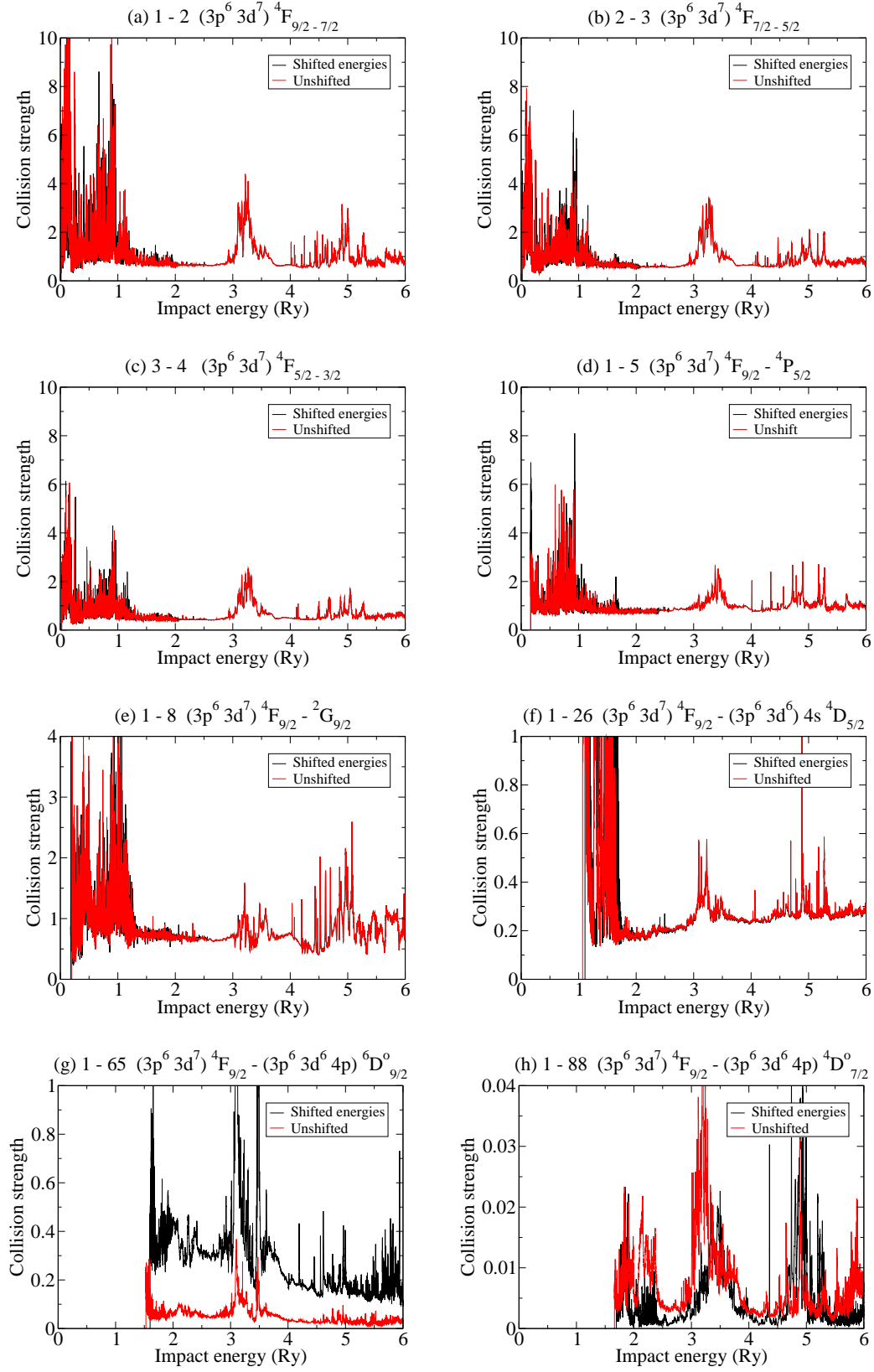


Figure 1. Electron-impact excitation collision strengths Ω of Ni^{3+} .

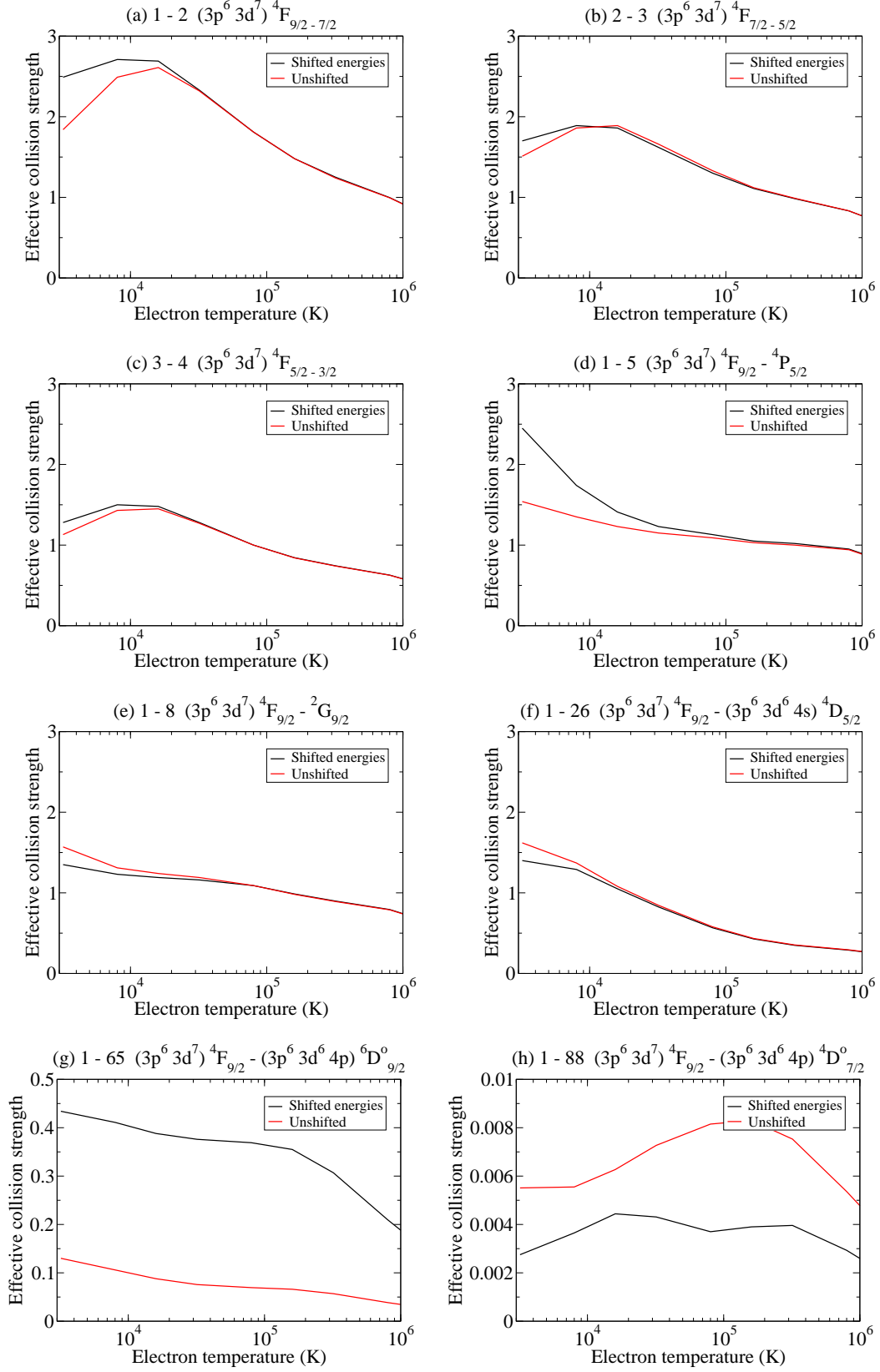


Figure 2. Electron-impact excitation effective collision strengths Υ of Ni^{3+} for a Maxwellian electron distribution.

atomic states have not been modified, but the energies have, since in one of them they have been shifted to the recommended values of NIST. As a consequence, the line strengths S have the same value in both calculations. At high energies, the collision strengths are determined by the infinite energy point, which in the case of E1 transitions depends only on the value of S , see [Burgess & Tully \(1992\)](#). In Figure 1 it is appreciated that for the E1 transition 1 – 65 the collision strengths obtained using both versions disagree at low impact energies, but they converge at high ones.

We present in Figure 2 the corresponding Maxwellian averaged effective collision strengths Υ_{ij} for the same transitions depicted in Figure 1, for a range of electron temperatures $T_e = 10^3 - 10^6$ K. Clearly evident is the strong enhancement of the collision rates due to the proper delineation of the Rydberg resonance features in the collision strengths. For the online material we provide tables of the calculated effective collision strengths for all the 34 191 transitions between all levels of Ni^{3+} . For non-Maxwellian modeling or for any application that requires the direct collision strengths we direct the reader to our public ftp server ⁶. We also refer to the OPEN-ADAS ⁷ data base for the general ADF04 file.

As a convergence test we have compared different ADF04 files, in the first one we have included in the partial wave expansion angular momenta up to $J = 30$ and no top-up, in a second one we have added the top-up to the $J = 30$ expansion, and finally our recommended data with the partial wave expansion extended up to $J = 36$ plus top-up. The largest differences remain between the versions with and without top-up, in that case the average difference between all the transitions values 0.5%. In particular for the E1 allowed transitions, the maximum difference reaches the 100%, while for the forbidden transitions this maximum difference is of the order 10%. If we add the top-up to the $J = 30$ expansion the differences reduce significantly, the average difference is reduced to the 0.02%, and the maximum difference for the E1 transitions to the 33%, and only in six E1 transitions is above the 10%, these six transitions are between very excited states, above 100, and they are irrelevant for the modeling. It is clear the calculation is properly converged in terms of the expansion in partial waves once the top-up is added, expansion up to $J = 30$ and $J = 36$ produce equal results.

4.2 Photoionization of Ni^{2+}

We have calculated level resolved photoionization cross sections of Ni^{2+} from its 20 lowest-energy levels for each J^π symmetry with $J = 0 - 4$ and even parity, to all the 262 final states of Ni^{3+} included in the CC expansion. In a stellar cloud most of the population of Ni^{2+} will occupy the ground level $3p^6 3d^8 {}^3F_4$ with only a small fraction populating the metastable levels of the ground term 3F_3 , 3F_2 and 1D_2 . In an usual stellar cloud these metastable levels contribute to the opacity much less than the ground state. In addition, the 1D_2 level is coupled to the 3F term through a spin-changing M1 / E2 transition with a very small transition probability. Table 4 shows the Einstein transition coefficients for transitions among the three first terms of Ni^{2+} taken from [Garstang \(1958\)](#). Clearly transitions between these levels are very weak, with A-values of the order of $10^{-1} - 10^{-2} \text{ s}^{-1}$. These levels can therefore be considered as metastable when included in an opacity model. The first

Table 4. Spontaneous emission coefficients for transitions between the lowest-excited levels of $\text{Ni}^{2+} 3p^6 3d^8$

Lower level	Upper level	Type	WL	A
3F_4	1D_2	E2	7 124.8	4.5 [–3]
3F_3	1D_2	M1 / E2	7 889.9	4.8 [–1]
3F_2	1D_2	M1 / E2	8 499.6	2.1 [–1]
3F_4	3P_2	E2	6 000.2	5.0 [–2]
3F_3	3P_1	E2	6 401.5	3.8 [–2]
3F_3	3P_2	M1 / E2	6 533.8	1.1 [–1]
3F_2	3P_0	E2	6 682.2	4.6 [–2]
3F_2	3P_1	M1 / E2	6 797.1	1.6 [–2]
3F_2	3P_2	M1 / E2	6 946.4	2.3 [–2]
1D_2	3P_0	E2	31 259	2.4 [–6]
1D_2	3P_1	M1 / E2	33 942	9.0 [–2]
1D_2	3P_2	M1 / E2	38 023	9.8 [–2]

Key: WL, wavelength in air (Å); A, Einstein spontaneous emission coefficient s^{-1} , $A [B]$ denotes $A \times 10^B$.
Data from ([Garstang 1958](#)).

odd level of Ni^{2+} is the $3p^6 3d^7 4p {}^5F_5$ state, with an excitation energy of $110\,213 \text{ cm}^{-1}$ with respect the ground state, see [Kramida et al. \(2018\)](#). All the levels below it are radiatively connected to the ground and metastable states through one or several forbidden E2 and M1 transitions. These transitions are known to be more intense as the level-energy difference is greater and hence terms above 1G will not be populated in a low-density cloud.

In Figure 3 we present the total photoionization cross section of Ni^{2+} from its ground state as a function of photon energy in Ry, as well as the seven lowest metastable levels. The cross section depicts a typical structure of large Rydberg resonances on a continuous background. In order to reproduce the high-energy region above approximately 5.5 Ry it is necessary to include more continuum functions and additional highly-excited levels in the CC expansion of the target. In the online material we provide a full table of fully resolved photoionization cross sections from the 20 lowest-excited levels of with $J = 0 - 4$ and even parity of Ni^{2+} to the 262 lowest-excited levels of Ni^{3+} . These cross sections can be considered of high-quality for photon energies up to 5.5 Ry and can be used for any opacity model.

In Figure 4 a test of convergence for the calculation is presented. We compare two calculations performed with the same atomic structure of the target. In the first one (black line) we included in the configuration basis set of the $(N + 1)$ -electron system all the configurations derived from the addition of one extra electron into all the available orbitals included in the expansion to those configurations listed in Table 1 and with an expansion of the continuum including $N_c = 20$ functions. In the second one (red line) the configuration set was reduced somewhat extracting from Table 1 the $3p^5 3d^7 5s$, $3p^5 3d^7 5p$, $3p^5 3d^7 6s$, $3p^5 3d^7 6p$, $3p^6 3d^5 4d^2$, $3p^6 3d^6 4d$, $3p^4 3d^9$ basis configurations to build the $(N + 1)$ -electron system expansion, and with $N_c = 13$ functions for the expansion of the continuum. Evidently, there is a very small difference between both calculations with respect to the background, the position of the resonances and their heights. We can be confident therefore that the present calculation has converged with regard to the target description, the size of the continuum basis and the mesh size adopted in the low-energy region. For higher photon energies above 5.5 Ry a similar guarantee of the accuracy of the cross sections cannot be

⁶ <http://web.am.qub.ac.uk/wp/apa/publications-data/>

⁷ <http://open.adas.ac.uk>

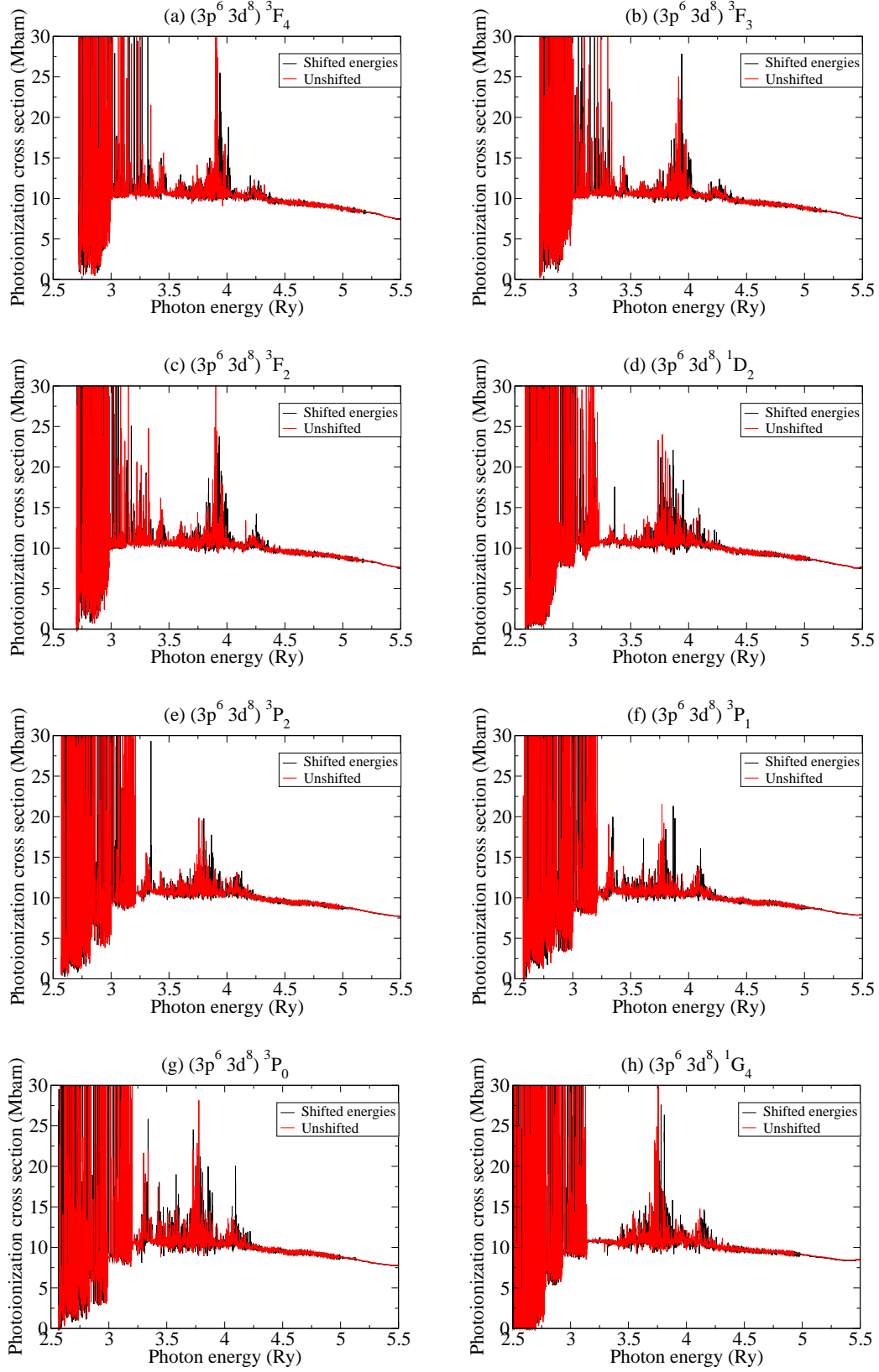


Figure 3. Photoionization cross sections versus the photon energy for Ni^{2+} from ground lowest-excited initial states. Colour online.

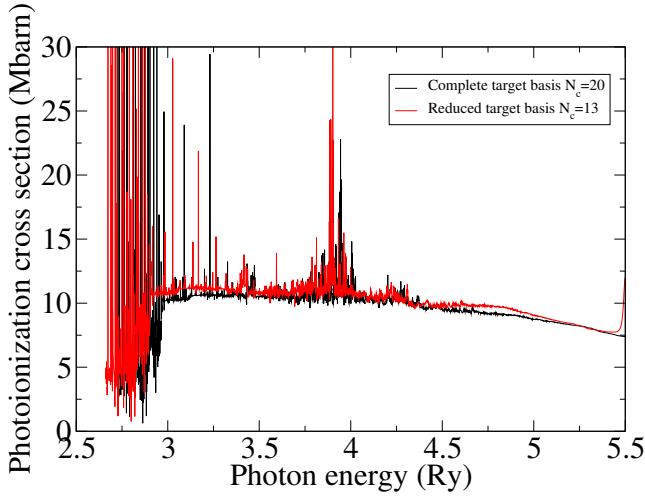


Figure 4. Photoionization cross section of Ni^{2+} ion initially in its ground state $3p^6 3d^8 {}^3F_4$ with two different expansions. Black line: calculation with the whole set of configurations and $N_c = 20$; Red line: calculation with a truncated set of configurations and $N_c = 13$.

made due to the effect of additional excited levels which are not included in our CC expansion.

As a test of accuracy we investigate in Figure 5 the relative difference of the photoionization cross sections produced when the target levels are shifted to their exact observed positions or left unshifted as the *ab initio* values. Relative differences of

$$\delta = \frac{\sigma_{sh} - \sigma_{un}}{\sigma_{sh}} \quad (3)$$

where σ represents the convoluted cross section with a Gaussian enveloping for several widths. The largest deviation occurs for the lower photon energies. For those energies the difference in the positioning of the resonances is the dominant contribution to the global error. For photon energies above 3 Ry, equivalent to wavelengths shorter than 303.76 Å, the relative deviation for the convolution with width 10^{-2} Ry remains below the 10% level in almost the entire domain. At a photon energy of $E = 3.81$ Ry the deviation reaches a maximum of 28%, just for a single resonance. For a convolution width of 10^{-3} Ry and photon energies above 3 Ry the relative difference remains below the 20% threshold. We estimate the accuracy of the present data to be approximately 20% in the worst case for wavelengths in the ultraviolet, above the ionization limit of Ni^{2+} .

5 MODELING OF DIAGNOSTICS.

With the calculated effective collision strengths for the electron-impact excitation of Ni^{3+} we have performed a collision-radiative model. We use the program COLRAD, which calculates the line intensities from the radiative transition probabilities and effective collision strengths stored in the `ADF04` file. For low densities, the only mechanism of population is the collisional excitation from the ground or a metastable state, following radiative-decay cascade. In Table 5 we have selected four line ratios to check their validity as diagnostics. These transitions were considered in a previous calculation by Pradhan & Zhang (1993) for the isoelectronic ion Fe^+ , and hence provide a benchmark for the current analysis.

The line intensity ratios are plotted in Figure 6 as a function

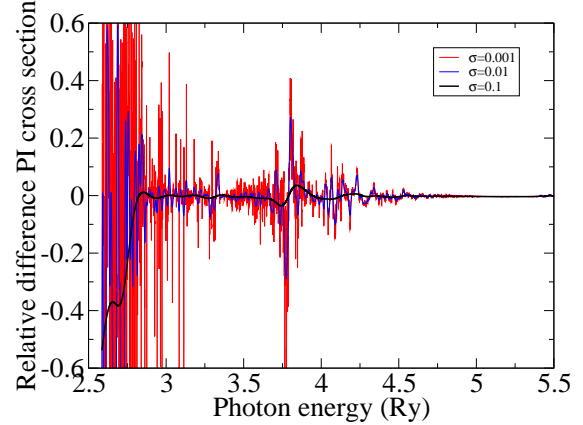


Figure 5. Relative difference of the photoionization cross section of Ni^{2+} from its ground level $3p^6 3d^8 {}^3F_4$ between shifted and unshifted versions of the calculation after several Gaussian convolutions with different widths. Colour online.

Table 5. Ni iv line ratios used for plasma diagnostics

Transition 1			Transition 2		
$i - j$	Levels	WL (Å)	$i - j$	Levels	WL (Å)
20 – 21	${}^6D_{9/2} - {}^6D_{7/2}$	127 345	1 – 2	${}^4F_{9/2} - {}^4F_{7/2}$	84 055
1 – 5	${}^4F_{9/2} - {}^4P_{5/2}$	5 519.2	4 – 7	${}^4F_{3/2} - {}^4P_{1/2}$	6 121.0
1 – 26	${}^4F_{9/2} - {}^4D_{5/2}$	821.0	1 – 25	${}^4F_{9/2} - {}^4D_{7/2}$	827.1
1 – 5	${}^4F_{9/2} - {}^4P_{5/2}$	5 519.2	20 – 25	${}^6D_{9/2} - {}^4D_{7/2}$	9 524.8

Key: WL, wavelength in vacuum, in Å.

of electron temperature and density. The ratio between the lines 1 – 5 and 20 – 25 ($5\,519.2\text{ Å}/9\,524.8\text{ Å}$) provides very powerful diagnostics for the electron temperature T . It is density independent and varies significantly in the range of the peak abundance temperature. The ratio 20 – 21/1 – 2 ($127\,345\text{ Å}/84\,055\text{ Å}$) similarly has a region where it is independent of density but the range is significantly greater than the temperature of maximum abundance for the Ni^{3+} ion. The ratio between lines 1 – 26 and 1 – 25 ($821.0\text{ Å}/827.1\text{ Å}$) is a very useful density diagnostic particularly for low density plasmas, below 10^9 cm^{-3} , in the range of the temperature of peak abundance. Additional line ratios can be analysed using the present effective collision strengths and with a more refined collision-radiative model. We provide good-quality data to perform plasma modeling using Ni iv emission lines.

For Fe II, the equivalent wavelengths to the ratio between 1 – 5 and 20 – 25 are the lines of 8 617.0 and 12 566.8 Å. The ratio of these lines can give a good diagnostics for the plasma temperature if it is in the range of the peak abundance for Fe^+ of $1.3 \times 10^4\text{ K}$, see (Smyth et al. 2018). Combining these two line ratios for Fe II and Ni IV we are able to determine with accuracy the electron temperature of the plasma in a wider range. In figure 7 we show the variation of these line ratios for the electron density of the Orion nebula.

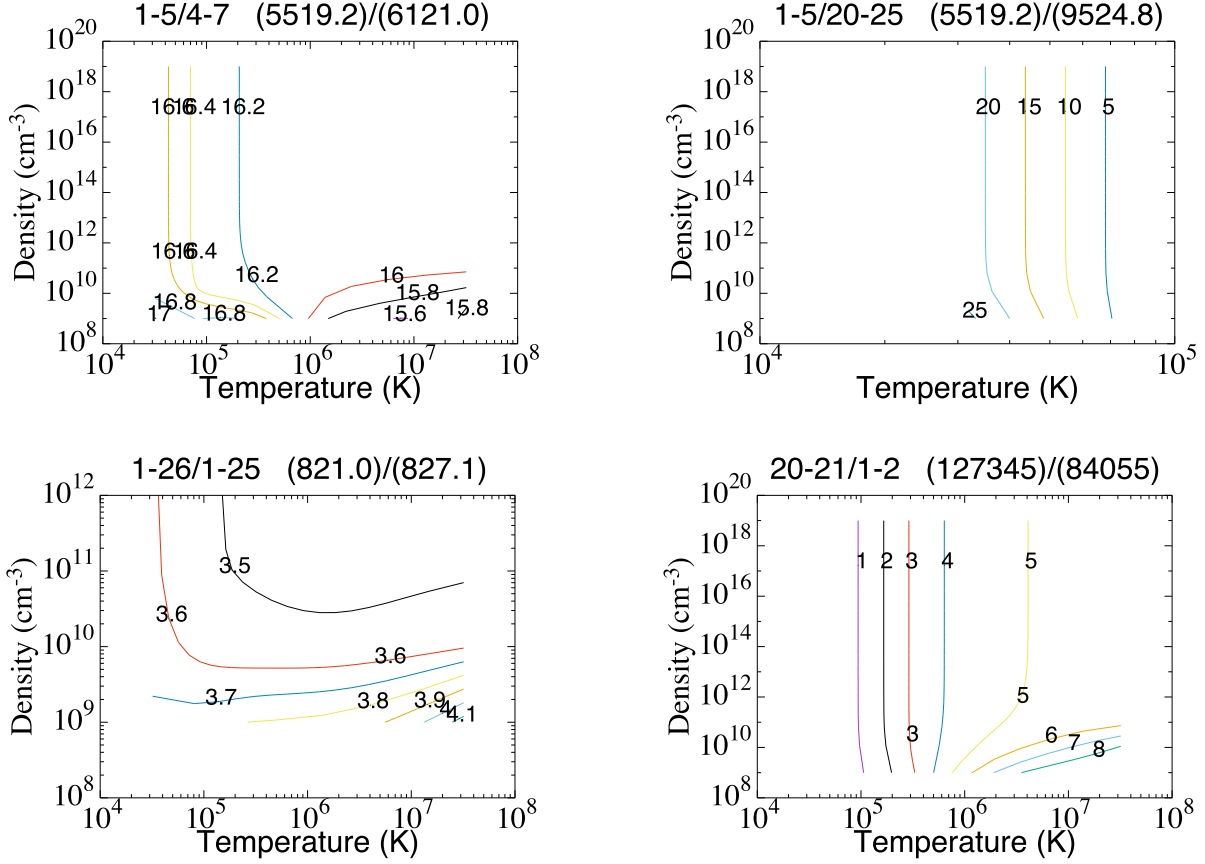


Figure 6. Line intensity ratio I_{11}/I_{12} versus electron temperature and density for some selected pairs of lines of Ni iv. Colour online.

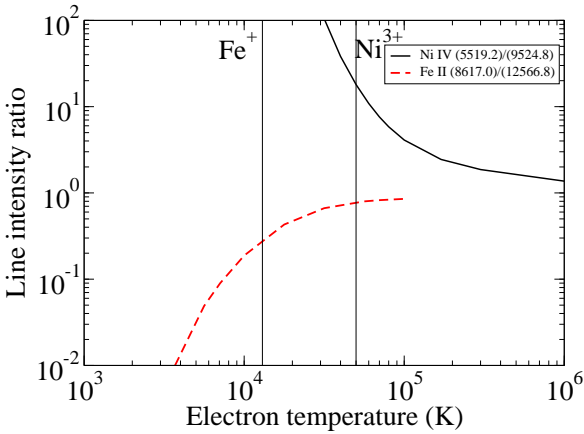


Figure 7. Line intensity ratio I_{11}/I_{12} versus electron temperature for a constant density of $d = 10^4 \text{ cm}^{-3}$ for lines (5 519.2 Å)/(9 524.8 Å) of Ni iv (full line) and (8 617.0 Å)/(12 566.8 Å) of Fe ii (dashed line). Vertical lines indicate the peak abundance temperature of each ion. Colour online.

6 CONCLUSIONS

We present high-quality atomic data for electron-impact excitation of Ni^{3+} and photoionization from the ground and metastable levels of Ni^{2+} . These data are essential for the interpretation of Ni iv lines collected from ground and satellite observations, as well as opacity due to Ni^{2+} in interstellar clouds. A fully relativistic Dirac atomic *R*-matrix code (DARC) treatment is adopted with a configuration interaction expansion of the 25-electron target Ni^{3+} incorporating lowest 262 levels in the close coupling expansion of the target. For each of the two processes we have performed two calculations, one using the calculated energies and atomic wave functions obtained within GRASP, and a second one replacing the calculated energies with the recommended data tabulated in the NIST database. For both processes, the differences between the two calculations performed was negligible with the background cross section as well as the height and positioning of the resonance structures almost identical in both. Accuracy checks were performed throughout the analysis and we are confident that the present data represents the best available to date for use by the astrophysics and plasma physics communities.

ACKNOWLEDGMENTS

Present work has been funded by the STFC through the QUB Astronomy Observation and Theory Consolidated Grant

ST/P000312/1. The computation has been performed in the supercomputer Hazelhen property of the Höchstleistungsrechner für Wissenschaft und Wirtschaft (Germany), and Archer property of the Engineering and Physical Science Research Council under the allocation E464-RAMPA.

This paper has been typeset from a \LaTeX file prepared by the author.

REFERENCES

- Ait-Tahar S., Grant I. P., Norrington P. H., 1996, *Phys. Rev. A*, 54, 3984
- Badnell N. R., 2011, *Comp. Phys. Comm.*, 182, 1528
- Badnell N. R., Griffin D. C., 2001, *J. Phys. B: At. Mol. Opt. Phys.*, 34, 681
- Bailey J. E., et al., 2014, *Nature*, 517, 56
- Ballance C. P., Griffin D. C., 2004, *J. Phys. B*, 37, 2943
- Bautista M. A., 2004, *Astron. Astroph.*, 420, 763
- Berrington K. A., Burke P. G., Butler K., Seaton M. J., Storey P. J., Taylor K. T., Yan Y., 1987, *J. Phys. B: At. Mol. Phys.*, 20, 6379
- Berrington K. A., Eissner W. B., Norrington P. H., 1995, *Comp. Phys. Comm.*, 92, 290
- Bryans P., Badnell N. R., Gorczyca T. W., Laming J. M., Mitthumsiri W., Savin D. W., 2006, *Astroph. J. Suppl. Ser.*, 167, 343
- Burgess A., 1974, *J. Phys. B: At. Mol. Phys.*, 7, L364
- Burgess A., Tully J. A., 1992, *Astron. Astroph.*, 254, 436
- Burke P. G., 2011, *R-Matrix of Atomic Collisions: Application to Atomic, Molecular, and Optical Processes*. Springer-Verlag, New-York
- Dyall K. G., Grant I. P., Johnson C. T., Parpia F. A., Plummer E. P., 1989, *Comp. Phys. Comm.*, 55, 425
- Ferland G. J., et al., 2017, arXiv:1705.10877v2
- Garstang R. H., 1958, *Mon. Not. R. Astr. Soc.*, 118, 234
- Hansen J. E., Raassen A. J. J., Uylings P. H. M., 1984, *Astroph. J.*, 277, 435
- Hummer D. G., Berrington K. A., Eissner W., Pradhan A. K., Saraph H. E., Tully J. A., 1993, *Astron. Astroph.*, 279, 298
- Iglesias C. A., Rogers F. J., 1996, *Astroph. J.*, 464, 943
- Kramida A., Yu. Ralchenko Reader J., and NIST ASD Team 2018, NIST Atomic Spectra Database (ver. 5.5.6), [Online]. Available: <https://physics.nist.gov/asd> [2018, June 27]. National Institute of Standards and Technology, Gaithersburg, MD.
- Mazzali P. A., Nomoto K., Cappellaro E., Nakamura T., Umeda H., Iwamoto K., 2001, *Astroph. J.*, 547, 988
- Mazzotta P., Mazzitelli G., Colafrancesco S., Vittorio N., 1998, *Astron. Astroph. Suppl. Ser.*, 133, 403
- McCray R., Fransson C., 2016, *Annual Review of Astronomy and Astrophysics*, 54, 19
- Moravveji E., 2016, *Mon. Not. R. Astr. Soc.*, 455, L67
- Norrington P. H., Grant I. P., 1981, *J. Phys. B: At. Mol. Phys.*, 14, L261
- Norrington P. H., Grant I. P., 1987, *J. Phys. B: At. Mol. Opt. Phys.*, 20, 4869
- Parpia F. A., Fischer C. F., Grant I. P., 1996, *Comp. Phys. Comm.*, 94, 249
- Pradhan A. K., Berrington K. A., 1993, *J. Phys. B: At. Mol. Opt. Phys.*, 26, 157
- Pradhan A. K., Zhang H. L., 1993, *Astroph. J.*, 409, L77
- Ramsbottom C. A., 2009, *At. Data Nucl. Data Tables*, 95, 910
- Ramsbottom C. A., Noble C. J., Burke V. M., Scott M. P., Kisieliński R., Burke P. G., 2005, *J. Phys. B: At. Mol. Opt. Phys.*, 38, 2999
- Ramsbottom C. A., Hudson C. E., Norrington P. H., Scott M. P., 2007, *Astron. Astroph.*, 475, 765
- Sánchez N., Alfaro E. J., Pérez E., 2007, *Astroph. J.*, 656, 222
- Seaton M., 1982, *Comp. Phys. Comm.*, 25, 87
- Smyth R. T., Ramsbottom C. A., Ballance C. P., 2018, *Mon. Not. R. Astr. Soc.*, p. submitted
- Sugar J., Corliss C., 1985, *J. Phys. Chem. Ref. Data*, pp 1–664
- Summers H. P., 1994, ADAS manual. JET Joint Undertaking
- The Opacity Project Team 1995, *The Opacity Project Vol. 1*. Institute of Physics Publications, Bristol, UK
- Werner K., Rauch T., Kruk J. W., 2018, *Astron. Astroph.*, 609, A107
- Zhang H. L., Pradhan A. K., 1995, *Astron. Astroph.*, 293, 953
- Zhang H. L., Pradhan A. K., 1997, *Astron. Astroph. Suppl. Ser.*, 126, 373